



# Automatic Organ Segmentation for CT Scans Based on Super-Pixel and Convolutional Neural Networks

Xiaoming Liu<sup>1</sup> · Shuxu Guo<sup>1</sup> · Bingtao Yang<sup>2</sup> · Shuzhi Ma<sup>3</sup> · Huimao Zhang<sup>4</sup> · Jing Li<sup>4</sup> · Changjian Sun<sup>1</sup> · Lanyi Jin<sup>1</sup> · Xueyan Li<sup>1</sup> · Qi Yang<sup>4</sup> · Yu Fu<sup>4</sup>

Published online: 20 April 2018

© Society for Imaging Informatics in Medicine 2018

## Abstract

Accurate segmentation of specific organ from computed tomography (CT) scans is a basic and crucial task for accurate diagnosis and treatment. To avoid time-consuming manual optimization and to help physicians distinguish diseases, an automatic organ segmentation framework is presented. The framework utilized convolution neural networks (CNN) to classify pixels. To reduce the redundant inputs, the simple linear iterative clustering (SLIC) of super-pixels and the support vector machine (SVM) classifier are introduced. To establish the perfect boundary of organs in one-pixel-level, the pixels need to be classified step-by-step. First, the SLIC is used to cut an image into grids and extract respective digital signatures. Next, the signature is classified by the SVM, and the rough edges are acquired. Finally, a precise boundary is obtained by the CNN, which is based on patches around each pixel-point. The framework is applied to abdominal CT scans of livers and high-resolution computed tomography (HRCT) scans of lungs. The experimental CT scans are derived from two public datasets (Sliver 07 and a Chinese local dataset). Experimental results show that the proposed method can precisely and efficiently detect the organs. This method consumes 38 s/slice for liver segmentation. The Dice coefficient of the liver segmentation results reaches to 97.43%. For lung segmentation, the Dice coefficient is 97.93%. This finding demonstrates that the proposed framework is a favorable method for lung segmentation of HRCT scans.

**Keywords** Organ segmentation · Super-pixels · CNN · SVM classifier · CT scans

✉ Xueyan Li  
leexy@jlu.edu.cn

Xiaoming Liu  
liuxm16@mails.jlu.edu.cn

Shuxu Guo  
guosx@jlu.edu.cn

Bingtao Yang  
yangbt16@mails.jlu.edu.cn

Shuzhi Ma  
981289164@qq.com

Huimao Zhang  
huimaozhanglinda@163.com

Jing Li  
1055407760@qq.com

Changjian Sun  
scjju@gmail.com

Lanyi Jin  
jinly15@mails.jlu.edu.cn

Qi Yang  
yangqi\_tt@163.com

Yu Fu  
fuyu-1985@163.com

<sup>1</sup> College of Electronic Science & Engineering, Jilin University, D451 Room of Tangaoqing Building, No. 2699 of Qianjin Street, Changchun, Jilin, China

<sup>2</sup> College of Communication Engineering, Jilin University, Changchun 130012, China

<sup>3</sup> LUSTER LightTech Group, Beijing, China

<sup>4</sup> Department of Radiology, The First Hospital of Jilin University, Changchun, China

## Introduction

CT is one of the most significant medical imaging technologies to assess the human body. Human CT scans contain abundant information, such as complex soft-tissues and vascular and multiple organs, including the liver, kidney, gallbladder, lung, and spleen. For computer-aided diagnosis, segmentation for the region of interest (ROI) in CT images is a key precondition. Therefore, seeking a generic method that can replace manual segmentation is urgent.

Several state-of-the-art algorithms, including thresholding, region-based methods, and graph cut, have been proposed to assist organ segmentation. Thresholding is one of the simplest and the most classical methods for segmenting images that are light objects on dark backgrounds. For example, Moltz [1] combined a threshold-based approach with morphological processing and achieved the accurate segmentation of liver tumors. Compared with other strategies, thresholding involved fewer calculations, but it does not account for the spatial characteristics, since it is sensitive to noise.

Region growing [2] is a typical application of region-based methods. This application is a procedure that clusters all the pixels into sub-regions according to a predefined criterion. For example, Devi K G [3] used a 3D regional growth method to distinguish between the kidneys, spleen, and three other organs. However, region growing is a method that depends on the seed region selection. Researchers usually select the seed points to improve the quality of segmentation. An adaptive regional growth method that learns the homogenous criteria from characteristics of the region was presented by [4]. However, the efficiency depends on the homogeneity of the tissue. Under-segmentation will occur when the target is inhomogeneous.

The core of graph cuts represents the image to an undirected weighted graph. Oda M [5] applied graph cut to four-organ segmentation. Graph cut is not always automatic, since it needs users to carefully select seed points labeled as the “object” and “background” [6].

Several machine learning-based attempts [7–9] have also been applied to the domain. Existing work in multi-organs segmentation can be roughly divided into registration-based and classification-based methods [10]. Several classification-based methods [11–13] used traditional classifiers to extract appearance features. Researchers in the field of medical imaging investigate the potential of deep learning in medical images acquired with CT, MRI, and PET [14]. Deep learning (DL) has shown promising accuracy as an automatic segmentation algorithm. Meanwhile, certain specific DL frameworks are primarily being performed for classification [15–17], objects detection (lesions, organs) [18–21], and segmentation [22, 23]. CNN [24] is an effective branch of deep artificial neural networks. Kayalibay [25] achieved effective segmentation of hand and brain MRIs using the CNN-based method.

Employing a similar approach, Cha K [26] segmented the bladder, and Zou Y [27] segmented several digestive organs.

In CNN-based semantic segmentation tasks, the patch-based method transforms segmentation into pixel-wise classification. The strategy improved segmentation with more precise outputs. However, in spite of the high classification accuracy, the traditional CNN cannot avoid poor results, which caused by huge input data. In other words, reducing data redundancy can promote segmentation. A novel CNN framework that provides substantial improvements using super-pixels and a support vector machines (SVM) is presented in this paper.

Abdominal CTs can reflect multiple organs; however, abdominal CTs can image only a part of the lung bases, and they cannot be used to detect most lung diseases due to the incomplete reflection. At present, a most common clinical tactic to detect lung disease is HRCT. HRCT enhances parameters to maximize the spatial resolution at the time of imaging. HRCT can clearly reflect lung tissue and is regarded as the first option for the diagnosis of pulmonary diffuse lesions.

For the two types of CT images, we emphasize determining the contours and then extracting entire regions of organs. The presented framework was verified using liver and lung segmentation with desirable outputs.

The next section provides details of the dataset and methods. The section after that describes the experimental results and the evaluation. Finally, we discuss and conclude the results.

## Materials and Methods

### Experimental Environment

The whole experiment was performed on a PC with Linux Ubuntu 14.04 LST 64-bit operating system with an Intel i3 3.6 GHz CPU (Intel Core i3-4160), 16 GB of memory and an NVIDIA GeForce GTX 960 graphics card. The CNN was trained and tested using the CAFFE deep learning library [28]. The algorithms (including the super-pixel and post-processes) are conducted on MATLAB 2016a software. Since LIBSVM is one of the most widely used SVM libraries of [29], the involved SVM classifier is based on LIBSVM 3.14.

### Materials

The experimental data are comprised of two parts: the liver dataset and the lung dataset.

The liver data comes from the public dataset Sliver 07 [30]. The dataset consists of abdominal CT scans from 20 anesthetized patients (more than 5500 liver slices) and regional annotations. The CT scans are in grayscale with  $512 \times 512$  pixels.

The lung data are gathered from the open Chinese dataset TIANCHI Medical AI Challenge [31]. The dataset is composed of 13 HRCT scans. The sum of CT images reaches to 5000 slices, and the CT slices are all in grayscale with  $512 \times 512$  pixels. The corresponding ground truths of all lung slices are marked by a specific group of 4 radiologists. The radiologists are all clinicians working at the First Hospital of Jilin University, China, and their experience levels are detailed as follows: Radiologist1 is a chief physician with 24 years of experience. Radiologist2 is an attending doctor with 13 years of experience. Radiologist3 is an attending doctor with 6 years of experience. Finally, Radiologist4 is a physician with 3 years of experience. The process of annotation is divided into two steps. In the initial blinded-read phase, each radiologist independently reviewed each CT slice and marked the lung region. In the subsequent unblinded-read phase, each radiologist independently reviewed their own marks along with the anonymous marks of the three other radiologists to render a final opinion.

Finally, we processed the two dataset via the “leave-one-patient-out” cross-validation tactic to divide the original dataset into a training set and a testing set.

## Methods

We intend to classify each pixel of the CT images via CNN. To reduce the input, the super-pixel and SVM classifier are introduced. Organ segmentation is executed in following manner. First, CT slices are decomposed into a set of disjointed super-pixels by the SLIC. Next, calculation is performed on each super-pixel region and a multi-elemental array is formed. The digital signature of the array contains divided mathematical criteria of the SLIC. These signatures represent the characteristics of different organs in abdominal CT images. Even if the selected organ is by itself, more information can be obtained from the figures. Compared to the ground truth, the selected super-pixels are divided into three parts: all-organ area (labeled as 1), mixed area (labeled as 0), and non-organ area (labeled as  $-1$ ). Then, ample labeled vectors are put into SVM classifier to train a model. Through the trained SVM model, all super-pixel blocks in the CT images could be automatically classified. The SVM reduces the computational efforts and identifies the initial liver boundary [32].

Consequently, we utilize the CNN to refine the rough edges. We treat a single pixel on an edge as the center and cut a specific sized patch around it. Next, the patches are fed into CNN, and a training model is obtained. The CNN model can achieve pixel-wise assorting and smooth the rough edges. To date, the desirable contours of organs in CT images have already been extracted through above procedure. Finally, the output from the CNN is post-processed. In this phase, several kinds of morphological treatments are manipulated to complete the outputs. Certain interrupted edges are connected by

close operation. Next, the closed areas are filled. The erosion operation is employed to eliminate thin protrusions and tiny isolated areas to obtain the final results. The above master steps can be viewed in the flow diagram in Fig. 1.

## SLIC

Within a super-pixel, pixels have similar colors, textures, and intensities [33]. SLIC [34] has been proven as a fast and effective method to generate super-pixels. SLIC proceeds in the following steps.

Step 1. Initializing the seed points. The sole parameter of the SLIC algorithm is  $K$ , which indicates the desired amount of the equally sized super-pixels. Assuming that the image includes a total of  $N$  pixels, then the size of each super-pixel grid is  $N/K$ . The approximate size of grids is

$$S = \sqrt{N/K} \quad (1)$$

Step 2. Assignment. Once each pixel  $i$  is related to the nearest cluster center; there is a step to update the center by adjusting the mean  $[l, a, b, x, y]^T$  vector, where  $l$  means light, and  $a$  and  $b$  represent the color changing trends. In the CIELAB color space, the information involving color is represented by the vector  $[l, a, b]^T$ , while the pixel's position is located by the vector  $[x, y]^T$ .

Step 3. Distance measurement. According to the presented vector, it is necessary to normalize color proximity and spatial proximity using the formulas

$$d_c = \sqrt{(l_j - l_i)^2 + (a_j + a_i)^2 + (b_j + b_i)^2} \quad (2)$$

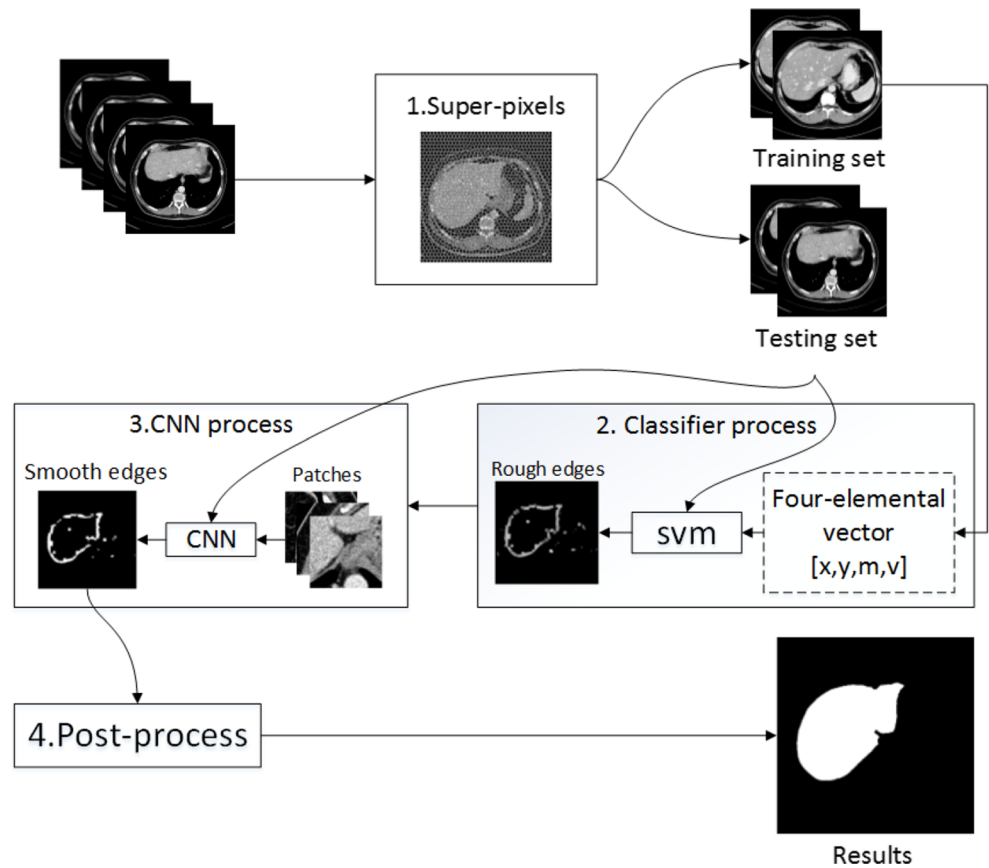
$$d_s = \sqrt{(x_j + x_i)^2 + (y_j + y_i)^2} \quad (3)$$

To combine the two distances into a single measure, the formula is defined as

$$D' = \sqrt{\left(\frac{d_c}{m}\right)^2 + \left(\frac{d_s}{S}\right)^2} \quad (4)$$

where  $S$  represents the interval between grids, and  $m$  is the balanced parameter used to weigh the proportions of color information and spatial information in this measurement. Finally, a separate number was assigned to each cluster on the basis of the computed distance.

**Fig. 1** Flow diagram of the main steps



Step 4. Connection. Disjointed pixels were redistributed to nearby super-pixels to enhance the connectivity.

Figure 2b shows the segmentation result when the parameter  $K$  equals 200. Super-pixel grids can be divided into three categories: all-organ areas (labeled as 1), non-organ areas (labeled as -1), and mixed areas (labeled as 0). Figure 2b exhibits the label assignment.

In the CIELAB color space, the pixels in the same super-pixel grid share similar digital signatures including color and spatial information, which are represented by a mean vector  $[l, a, b, x, y]^T$ . However, in grayscale images, the expression of  $[l, a, b]^T$  would be invalid. We employ the mean and variance of

grayscale values in each super-pixel grid to indicate the fluctuation of grayscale color. Therefore, the mathematical trait is re-denoted by the vector  $[x, y, m, v]^T$ , in which  $m$  and  $v$  are the mean and variance respectively.

The selection of the parameter  $K$  can be pivotal, since it directly determines the number of vectors. A small size cannot provide a sufficient signature, and an overly large size will increase complexity and cause over-fitting. With respect to the accuracy of the SVM on the liver dataset, we assess it with a  $K$  range of 200–2000 with an interval of 200. The accuracy trend is shown in Fig. 3. We notice that the accuracy steadily increases between  $K = 200$  and  $K = 1000$ , and then slightly fluctuates from  $K = 1200$  to  $K = 2000$ . Therefore, we carry

**Fig. 2** a Original image. b Illustration image with labeled super-pixel when  $K = 200$

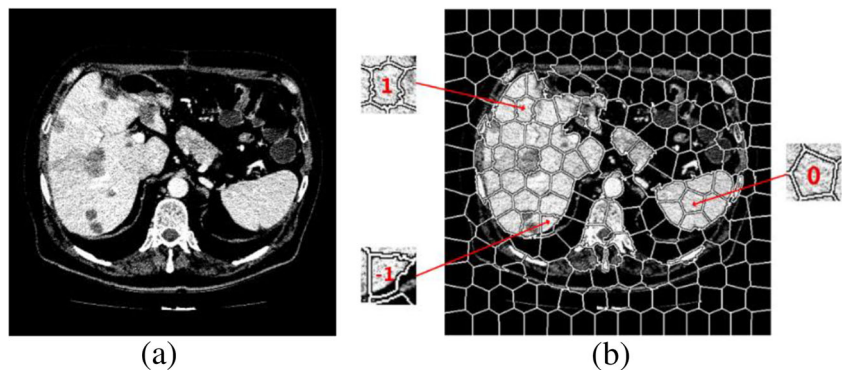
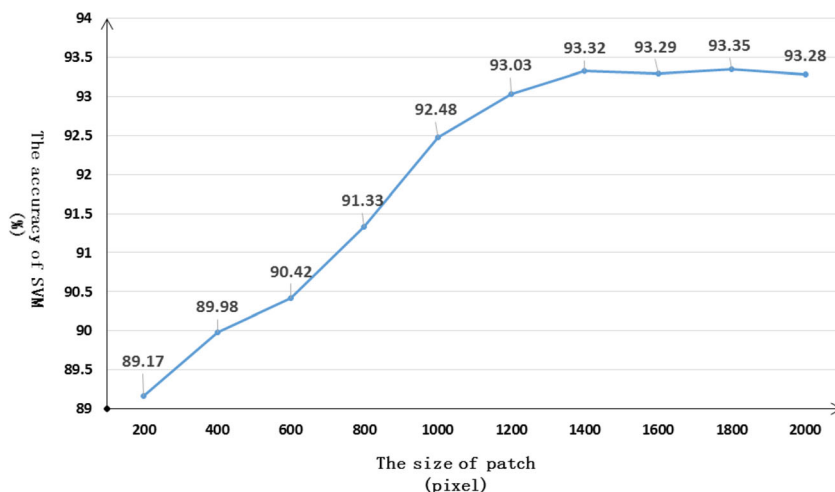


**Fig. 3** Rough line chart of selection of  $K$



out another detailed comparison from  $K = 1200$  to  $K = 2000$  with an interval of 100. The second accuracy trend is displayed in Fig. 4. It is obvious that the optimal selection is when  $K = 1500$ . An exemplary output of SLIC is shown in Fig. 5.

**SVM Classifier**

SVM is a statistically robust learning method based on structural risk minimization [35]. When solving small-sample, non-linear, and multi-dimensional data in our experiment, the SVM classifier displays unique advantages.

As the name implies, the SVM classifier demands vectors. The extracted features adapt to this requirement. The target of the SVM is to find an optimal solution to the hyper-plane and separate the data among 3 classes (1, 0, and -1). Each training data instance consists of a  $(p_i, q_i)$  pair, and we defined the pair as

$$p_i = [x_i, y_i, m_i, v_i]^T, i = 1 \cdots N \tag{5}$$

$$q_i = \begin{cases} 1 \\ 0 \\ -1 \end{cases}, i = 1 \cdots N \tag{6}$$

where  $i$  represents the  $i$ -th vector, and  $N$  is the total number of vectors.

For the given pairs, selecting the appropriate parameters for LIBSVM would directly affects the accuracy. First, parameter  $s = 0$  represents the classification mode. Since the scale of the extracted features is not large, it is unnecessary to reflect the limited features to a high dimensional space. Therefore, the kernel function is set to RBF and parameter  $t$  is 2. Parameter  $\nu = n$  represents the  $n$ -fold cross-validation tactic and we adopt  $\nu = n = 10$ . For classification, the four elements play equal roles so that  $w = 1$ .

Otherwise, the precision depends on the site of gamma (parameter  $g$ ) and cost (parameter  $c$ ). To locate the appropriate parameters of  $c$  and  $g$ , a piece of brief code about parameter optimization is introduced. The details are exhibited in Algorithm 1.

**Fig. 4** Detailed line chart of the selection of  $K$

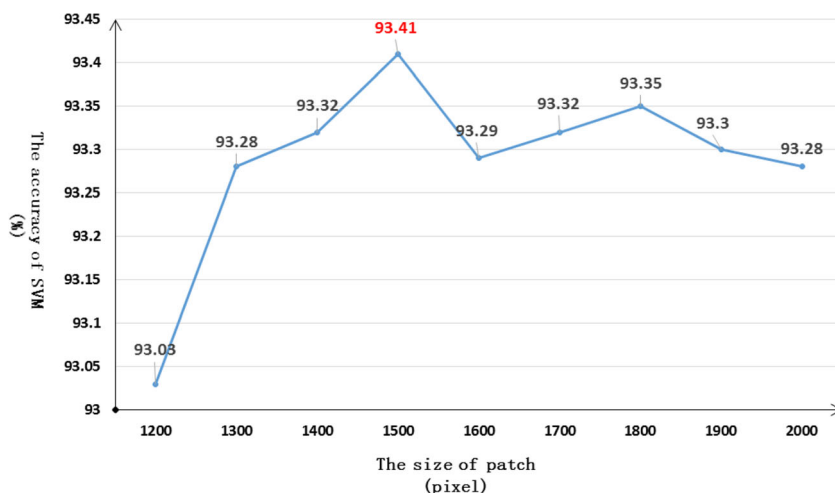
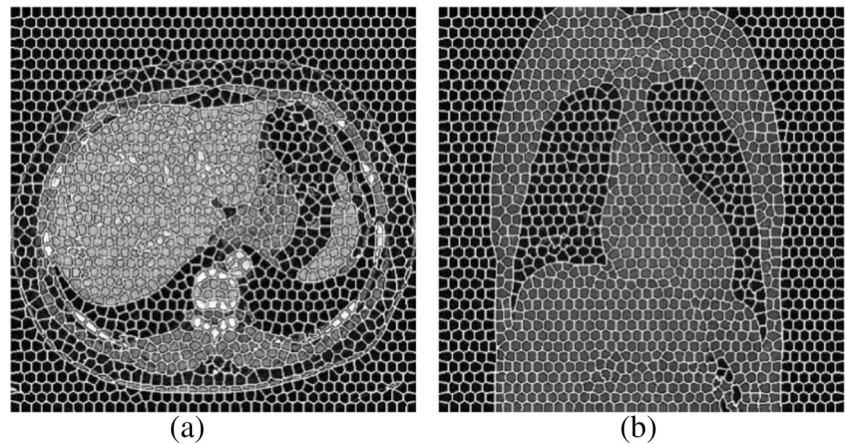


**Fig. 5** **a** Liver segmentation result of SLIC when  $K = 1500$ . **b** Lung segmentation result of SLIC when  $K = 1500$




---

**Algorithm 1** Parameter optimization on  $c$  and  $g$ .  $N$  is the maximum number of iterations, we used  $N=100$ ;  $Step\_size$  is the increased interval once, we used  $Step\_size=0.1$ , and  $Step\_size$  is growing in the range of  $[0, 5]$ ;  $cmd$  is a parameter list in string form,  $cmd='s=0, t=2, w=1, v=10'$ ;  $data$  is the four-elemental vectors that are extracted from the super-pixels;  $label$  is that corresponds to each vector.

---

$c=0, g=0$ ;

Getting the initial  $best\_accuracy$  by training SVM with the input data, label and parameter list: ‘ $cmd + c, g$ ’;

**for**  $N$  **do**

**for**  $Step\_size \in [0, 5]$  **do**

    Generating accuracy by training SVM with the input data, label and parameter list: ‘ $cmd + c=c+Step\_size, g$ ’;

**if**  $accuracy > best\_accuracy$  **do**

$best\_accuracy = accuracy$ ;

$best\_c = c$ ;

**end if**

    Generating accuracy by training SVM with the input data, label and parameter list: ‘ $cmd + best\_c, g=g+Step\_size$ ’;

**if**  $accuracy > best\_accuracy$  **do**

$best\_accuracy = accuracy$ ;

$best\_g = g$ ;

**end if**

**end for**

**end for**

print  $best\_c, best\_g$ ;

---

Algorithm 1 realizes the best accuracy when  $g = 1.2, c = 2.7$ .

Using the optimal combination of selected parameters, the SVM separates the super-pixels of the testing scans into 3 classes: all-organ area (labeled as 1), mixed area (labeled as 0), and non-organ area (labeled as  $-1$ ). Finally, among the target of edges collection, only the grids labeled as 0 are reserved for the further refinement.

## CNN

CNN is a popular branch of deep learning. In 2012, Alex Krizhevsky [36] proposed a classical CNN model, which was called AlexNet by the scholars in this field.

AlexNet consists of five convolutional layers (Conv1~Conv5), three max-pooling layers (Pool1, Pool2,

**Table 1** Parameters of the proposed CNN

| Layer | Kernel | Stride | Pad | Output size   |
|-------|--------|--------|-----|---------------|
| Data  | –      | –      | –   | 99 × 99       |
| Conv1 | 11     | 4      | 0   | 23 × 23 × 64  |
| Pool1 | 8      | 1      | 0   | 16 × 16 × 64  |
| Conv2 | 5      | 1      | 2   | 16 × 16 × 128 |
| Pool2 | 4      | 2      | 0   | 7 × 7 × 128   |
| Conv3 | 3      | 1      | 1   | 7 × 7 × 256   |
| Conv4 | 3      | 1      | 0   | 5 × 5 × 256   |
| Conv5 | 3      | 1      | 1   | 5 × 5 × 200   |
| Pool5 | 3      | 2      | 0   | 2 × 2 × 200   |
| Fc1   | –      | –      | –   | 2 × 2 × 128   |
| Fc2   | –      | –      | –   | 2 × 2 × 32    |
| Fc3   | –      | –      | –   | 2 × 2 × 2     |

and Pool5) and three fully connected layers (Fc1–Fc3). We adopt the original structure, loss function, optimizer, and most parameters except for the *num-output* of the traditional AlexNet. The parameter *num-output* represents the numbers in each layer. *Num-output* should be adjusted so that the model can be better adapted to the input. The details of the resetting are shown in Table 1, and the revised structure is exhibited in Fig. 6.

To improve the performance of the architecture, we need to collect a large amount of pixels to make it more powerful and intelligent. Therefore, splitting out patches of the detected edges is an ideal solution. The AlexNet captures information from patches, simplifies the sources, and exports feature maps layer by layer. The size of a patch directly influences the “receive filed” of the aftermost feature map.

In the framework of CAFFE, the length of the “receive filed” in each layer can be calculated as

$$L = \frac{Input + 2 * Pad - Kernel}{Stride} + 1 \quad (7)$$

For the input of  $512 \times 512$  pixels, each super-pixel contains approximately 175 pixels when  $K = 1500$ . Since the CNN is performed based on super-pixels, the final “receive filed” should be smaller than the average area of the super-pixels. In other words, the maximum of the length is  $\sqrt{175} \approx 13$  pixels. The other correspondence can be found in Table 2.

**Table 2** Correspondence between the size of patch and the area of final “receive filed”

| The size of patch (pixels) | The area of receive filed (pixels <sup>2</sup> ) | The size of patch (pixels) | The area of receive filed (pixels <sup>2</sup> ) | The size of patch (pixels) | The area of receive filed (pixels <sup>2</sup> ) |
|----------------------------|--|----------------------------|--|----------------------------|--|
| 275                        | 13 × 13  | 195                        | 8 × 8  | 115                        | 3 × 3  |
| 259                        | 12 × 12  | 179                        | 7 × 7  | 99                         | 2 × 2  |
| 243                        | 11 × 11  | 163                        | 6 × 6  | 83                         | 1 × 1  |
| 227                        | 10 × 10  | 147                        | 5 × 5  | –                          | –  |
| 211                        | 9 × 9  | 131                        | 4 × 4  | –                          | –  |

With respect to the accuracy of CNN on the liver dataset, we try every sized of patch mentioned in Table 2. The accuracy is shown in Fig. 7.

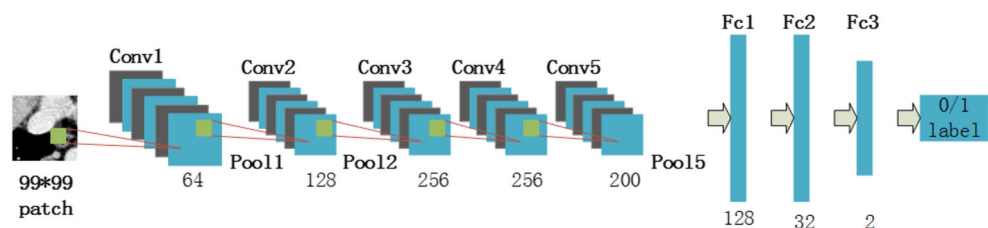
After repeated experiments, the patches whose size is 99 pixels are located at the highest rate of accuracy. The square patches are cut from the original CT images with a size of  $99 \times 99$  pixels<sup>2</sup>. It is a reasonable size, since there need to be enough big regions for the CNN to distinguish boundaries and ensure it is the target boundary. These patches are centered at every point on the boundary, which is selected by the mixed super-pixels in the section [Materials and Methods-SVM](#). Some patches are given in Fig. 8.

We used an untrained CNN with the above structure of AlexNet structure. The patches are trained on CAFFE with randomly initial weights. Based on the trained model, the points on the rough boundary are sorted into two kinds: points of organ region (labeled as 1) or points of background region (labeled as 0). When all the organ regions are maintained, smooth edges are effectively obtained.

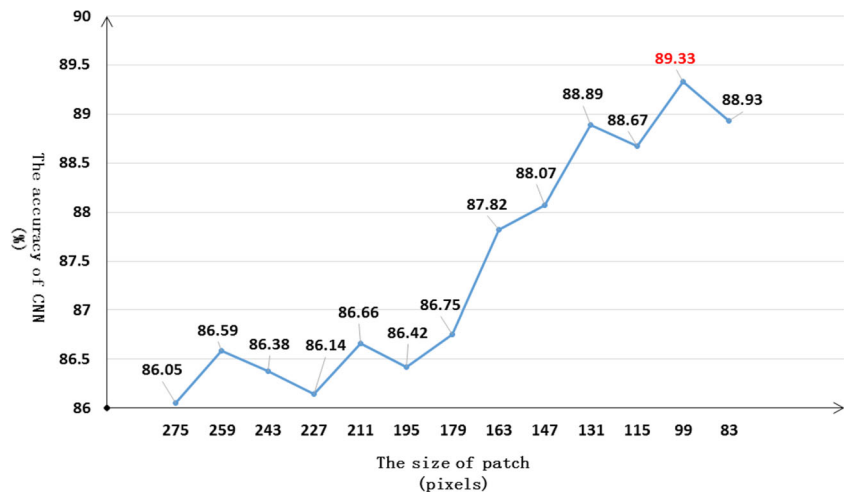
## Post-process

The presented segmentation method is emphasized on contour extracted. However, there are some flaws in the obtained boundary, including slight interruption and tiny errors in predicted regions, as shown in Fig. 9. Therefore, we applied some morphological operations to correct for the deviation.

The *open* operation is used to remove isolated regions, and the *close* operation is used to connect breakpoints on the border. Finally, we acquire closure on the contour. Then, the inner

**Fig. 6** Structure of the proposed CNN

**Fig. 7** Line chart of the selection of the patch size



area is filled and the segmentation result is obtained (Fig. 10d).

**Evaluation Metrics**

Dice’s similarity coefficient [37] can directly reflect the similarity between the segmentation result and the ground truth. It is considered as a most common metric when evaluating the accuracy of the segmentation algorithm. It can be calculated as

$$Dice = \frac{2|A \cap B|}{|A| + |B|} \tag{8}$$

**Evaluation Metrics on Liver Dataset**

The mean Dice of the final results reaches to 97.43% on the liver dataset.

However, in order to highlight different aspects of segmentation quality and acquire a comprehensive assessment, a variety of different measures should be employed. According to the literature [38], a scoring system is proposed for liver segmentation.

The score is defined as

$$\phi_i = \max\left(100 - 25 \frac{\varepsilon_i}{\bar{\varepsilon}_i}, 0\right) \tag{9}$$

$$\phi = \frac{1}{N} \sum_{i=1}^N \phi_i \tag{10}$$

where  $\phi$  represents final score,  $\phi_i$  is the score computed for each individual output slice,  $\varepsilon_i$  is the actual value of the corresponding metric for each output slice, and  $\bar{\varepsilon}_i$  is the mean of all outputs.

The described scoring system was employed with the following five error measures: volumetric overlap error (VOE) [39], relative volume difference (RVD), average symmetric surface distance (ASD), maximum symmetric surface distance (MSD), and root mean square symmetric surface distance (RMSD). These metrics are defined by the expressions

$$VOE = 1 - \frac{|A \cap B|}{|A \cup B|} \tag{11}$$

$$RVD = \pm \frac{|A| - |B|}{|B|} \tag{12}$$

$$ASD = \frac{1}{|B_1| + |B_2|} \left( \sum_{x \in B_1} d(x, B_2) + \sum_{y \in B_2} d(y, B_1) \right) \tag{13}$$

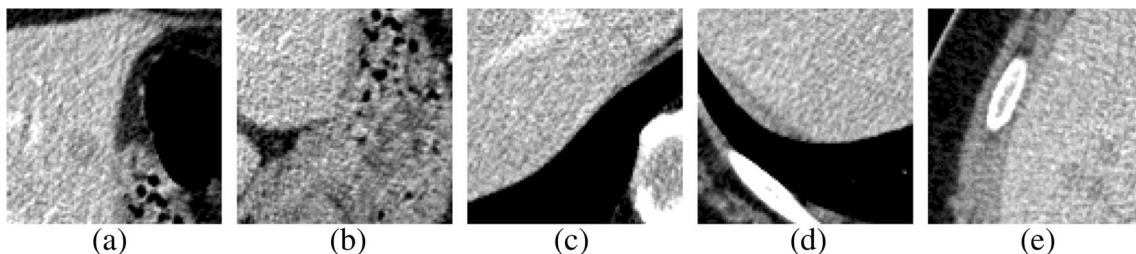
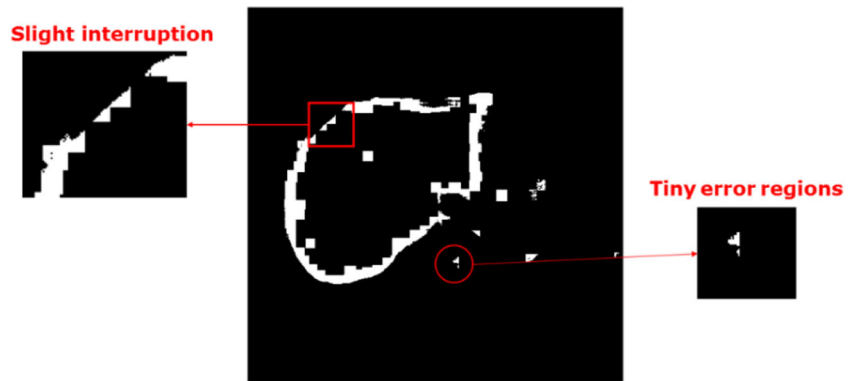


**Fig. 8** a–e Illustrations of extracted patches



**Fig. 9** An example of the flaws



$$MSD = \max \left\{ d_H(B_1, B_2), d_H(B_2, B_1) \right\} \quad (14)$$

$$RMSD = \sqrt{\frac{1}{|S(A)| + |S(B)|}} \sqrt{\sum_{s_B \in S(B)} d^2(s_B, S(A))} \quad (15)$$

where  $A$  represents the segmentation results, and  $B$  represents the ground truth.  $B_1$  represents the boundary of the result,  $B_2$  represents the boundary of the ground truth,  $S(A)$  represents the area of the resulting image, and  $S(B)$  represents the area of the ground truth.

Among these metrics, VOE is 0 for a perfect segmentation and 1 if segmentation and reference do not overlap at all. RVD reveals whether a method tends to over-segment or under-segment, where a value of 0 means that both volumes are

identical. RMSD is sensitive to outliers and returns the true maximum error. For RMSD, ASD, and MSD, 0 represents a perfect segmentation.

## Results

### Result on Liver Dataset

The accuracy of the SVM is enhanced by the parameter adjustment in Table 3.

The accuracy of the SVM classifier on the liver testing set reaches  $93.41 \pm 0.59\%$ . The accuracy of CNN is  $89.33 \pm 1.12\%$ . An example of the results is shown in Fig. 10.

**Fig. 10** **a** Original image, **b** rough liver boundary from SVM, **c** liver boundary from CNN, **d** liver segmentation result from the presented framework, **e** liver segmentation result from patch-based CNN only, and **f** liver ground-truth image

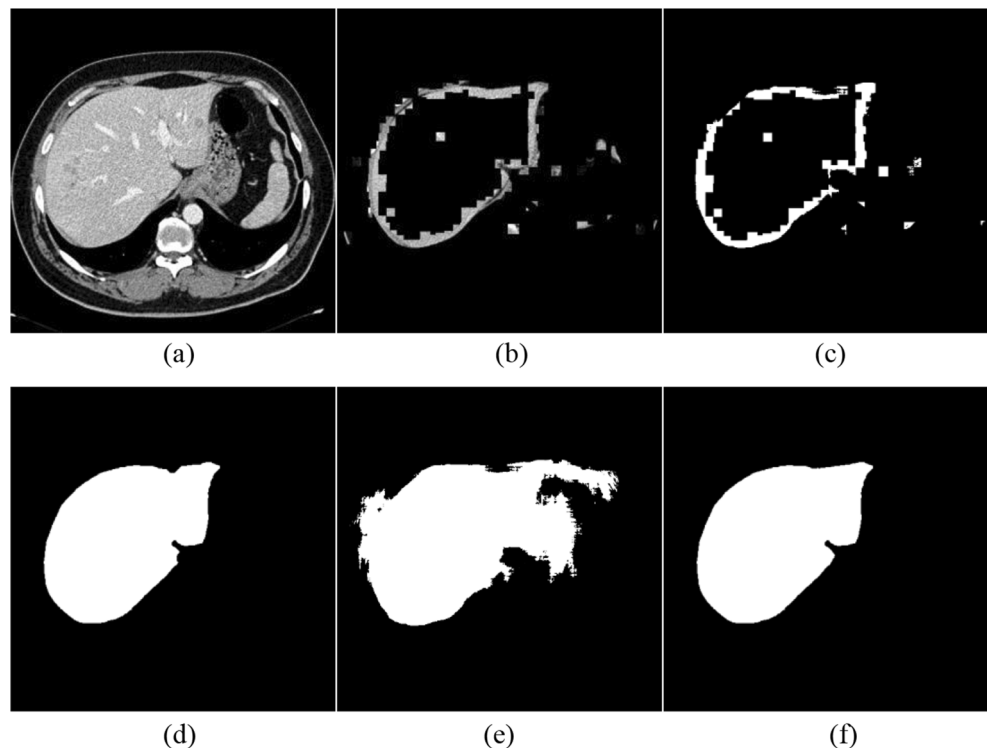


**Table 3** Parameters setting of LIBSVM

| Parameters | <i>s</i> | <i>t</i> | <i>g</i> | <i>c</i> | <i>w</i> | <i>v</i> |
|------------|----------|----------|----------|----------|----------|----------|
| Value      | 0        | 2        | 1.2      | 2.7      | 1        | 10       |

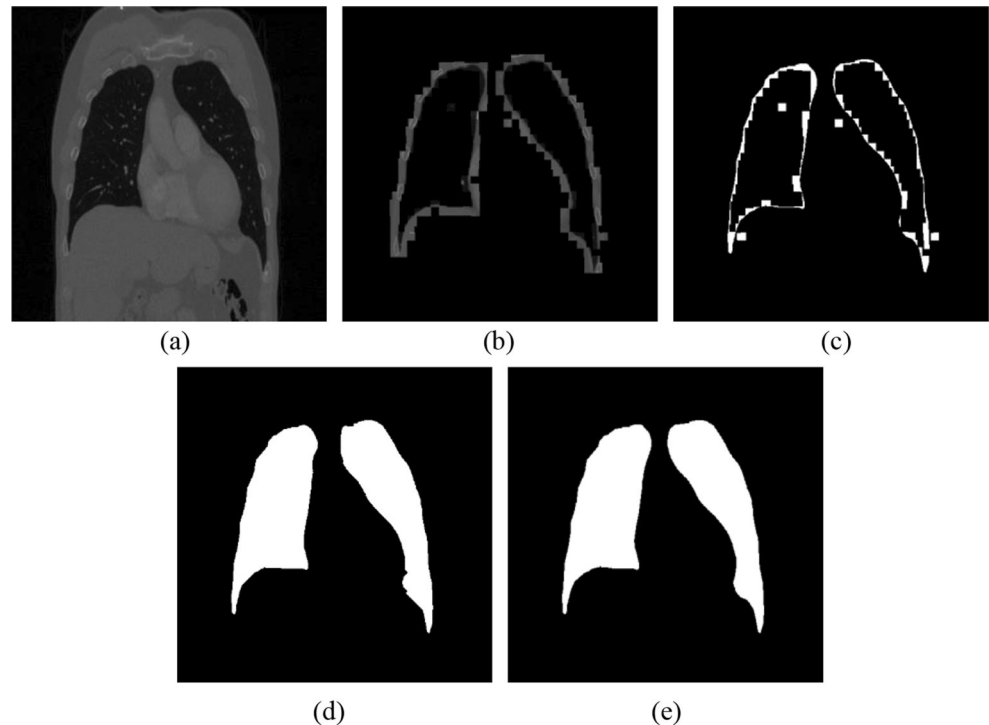
From Fig. 10, it is intuitive to observe that the results are very close to the true case. The results show that the pre-processing of the super-pixel and SVM promotes segmentation. Figure 10e is an output of the same CNN model, but the testing patches are cut from all pixels of the original CT image. Though accuracy of the trained CNN does not change, the false predictions are increased actually with the large-scale input. The comparison demonstrates that the pre-processing effectively reduces input redundancy.

### Result on Lung Dataset

The accuracy of the SVM classifier on the lung testing set is  $92.9 \pm 0.83\%$ . The accuracy of the CNN reaches  $91.8 \pm 1.37\%$ . An example of the results of lung segmentation is shown in Fig. 11.

From the lung segmentation result of Fig. 11, we can conclude that the presented framework can maintain the integral and symmetrical of the segmentation for both the left lung and the right lung.

**Fig. 11** **a** Original image, **b** rough lung boundary from SVM, **c** lung boundary from CNN, **d** lung segmentation result from the presented framework, and **e** lung ground-truth image



## Evaluation

### Evaluation on Liver Dataset

For the same datasets, the proposed framework is comparable to the state-of-art methods. Table 4 displays a further comparison among the other methods.

The above methods were all performed using the same dataset as ours. [40, 41, 45] adopted traditional methods. [42–44] proposed methods based on DL. Table 3 summarizes that the presented framework is better with lower time consumption. Compared to [44, 45], the proposed method improves accuracy. Compared to [40–43], in the case of similar scores, the proposed method reduces the processing time.

To test the segmentation performance for different liver shapes, we divide the testing set into 10 subsets. Each subset shares a similar form or liver size. The scale of each subset is unequal, and the number of slices ranges from 87 to 411. Instances of liver regions in some subsets are shown in Fig. 12. Table 4 records the performances in subsets 1–10.

In Table 5, the average areas liver is a metric used to measure the relative liver size of different subsets. Table 5 also shows the fluctuation of the six measurements by average and variance. The value of mean Dice is 97.1%, with the other five metrics being reasonable. It reveals that the method is steady and can well adapt to various liver forms.

**Table 4** Liver segmentation results comparison

| Method    | Runtime (s/slice) | VOE (%) | RVD (mm) | ASD (mm) | MSD (mm) | RMSD (mm) | Score |
|-----------|-------------------|---------|----------|----------|----------|-----------|-------|
| Ref. [40] | 135               | 5.35    | −0.17    | 0.84     | 19.58    | 1.78      | 80.3  |
| Ref. [41] | 90                | 5.42    | 1.75     | 0.79     | 33.55    | 1.87      | 76.2  |
| Ref. [42] | 285               | 6.24    | 1.18     | 1.03     | 18.82    | 2.11      | 77.9  |
| Ref. [43] | 120–180           | 4.58    | 1.08     | 0.68     | 16.88    | 1.45      | 83.4  |
| Ref. [44] | 27                | 7.87    | 1.31     | 1.29     | 23.56    | 2.50      | 71.4  |
| Ref. [45] | 24–184            | 5.90    | 2.70     | 0.91     | 18.94    | 1.88      | 77.8  |
| Ours      | 38                | 6.17    | 1.33     | 1.48     | 17.80    | 2.19      | 78.1  |

### Evaluation on Lung Dataset

We applied a novel segmentation framework on a lung dataset. According to formula (8), the mean Dice of the final results reaches 97.93%. Processing a slice requires 40 s.

Most existing studies on lung segmentation are performed on local datasets. To avoid unfair comparisons, we provide with a rough contrast [46] and [47] adopt traditional methods. The mean Dice of [46] is 98.62%, and the mean Dice of [47] is 93.7% [48] proposes a method based on DL and obtains a mean Dice of 98.5%. From there results, we can conclude that

the presented framework works well on both abdominal CTs and HRCTs.

### Discussion

In clinical applications, automatic segmentation methods that can detect multiple targets would be convenient for medical staff and benefit patients. The presented framework is accomplished-based liver and lung segmentations from CT scans.

**Fig. 12** **a** An example slice with the ground truth in subset 2, **b** an example slice with the ground truth in subset 3, **c** an example slice with the ground truth in subset 6, and **d** an example slice with the ground truth in subset 7

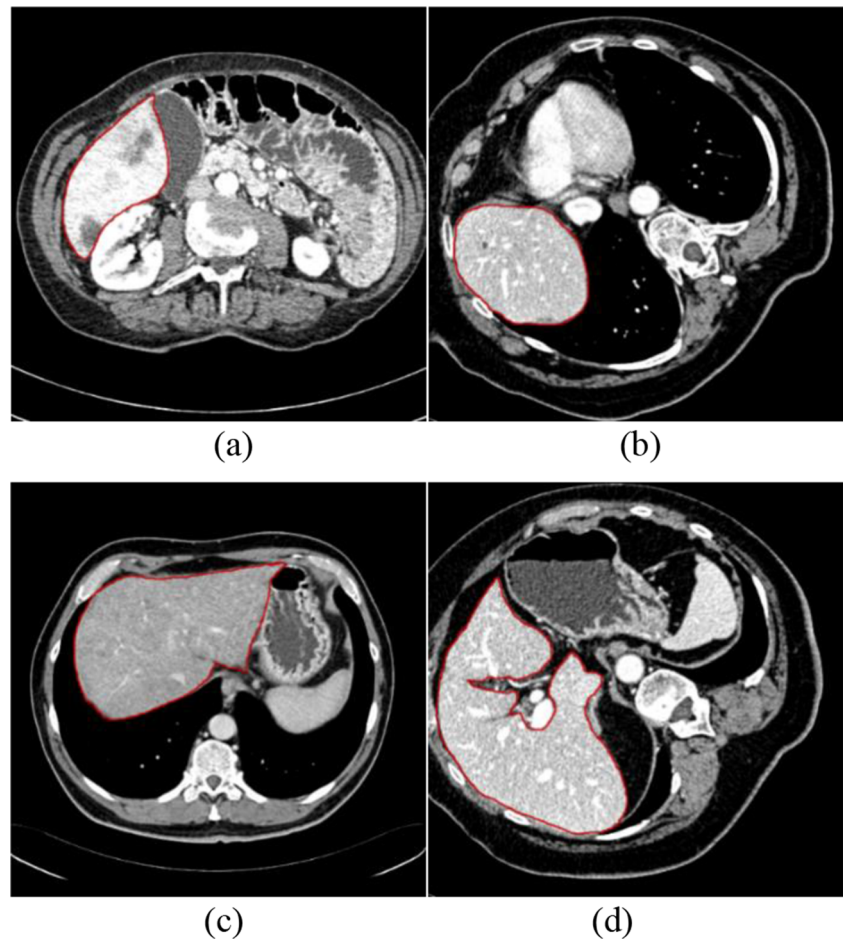


**Table 5** Results for livers of different sizes

| Number   | Average liver areas (pixels/slice) | Dice (%) | VOE (%) | RVD (%) | ASD (mm) | MSD (mm) | RMSD (mm) |
|----------|------------------------------------|----------|---------|---------|----------|----------|-----------|
| 1        | 10,137                             | 96.5     | 6.61    | −2.48   | 1.40     | 17.34    | 2.55      |
| 2        | 13,071                             | 96.2     | 6.67    | −1.25   | 1.19     | 16.21    | 2.37      |
| 3        | 22,672                             | 97.9     | 5.93    | 2.00    | 1.04     | 16.29    | 2.21      |
| 4        | 22,955                             | 98.3     | 5.68    | −0.72   | 1.13     | 15.67    | 2.14      |
| 5        | 26,685                             | 96.8     | 6.31    | 1.78    | 1.06     | 16.99    | 2.48      |
| 6        | 33,017                             | 97.3     | 5.97    | −1.89   | 1.22     | 16.45    | 2.25      |
| 7        | 47,535                             | 98.2     | 5.03    | 1.33    | 0.71     | 15.93    | 1.89      |
| 8        | 47,860                             | 96.3     | 6.86    | 1.79    | 1.47     | 16.19    | 2.37      |
| 9        | 49,533                             | 96.9     | 6.02    | −1.38   | 1.15     | 16.71    | 2.41      |
| 10       | 55,095                             | 97.0     | 5.21    | 1.13    | 1.27     | 16.24    | 1.99      |
| Average  | –                                  | 97.1     | 6.03    | 0.03    | 1.16     | 16.40    | 2.27      |
| Variance | –                                  | 0.76     | 0.61    | 1.73    | 0.21     | 0.49     | 0.21      |

We verified the framework on two different CT forms, the abdominal CT and the HRCT. In abdominal CT images, the discrimination between the liver and surrounding tissues are usually unclear due to low resolution, and the shapes and locations of livers are not always regular. Nonetheless, the HRCT is a CT imaging method with enhanced resolution. The desirable output of our method is a testimony to the flexibility for both high and low resolutions. In procedure of liver segmentation, the Dice coefficient reaches 97.43%. Table 4 demonstrates that the performance of the presented framework is comparable to other single-purpose methods. For the exploration of segmentation performances for different liver shapes, Table 5 proves that our method is robust.

We also made an attempt to segment lungs for HRCT using the proposed framework. All related parameter settings are the same with liver segmentation. The mean Dice of the final results reaches 97.93%. From the output shown in Fig. 11d, the morphology of the obtained lungs is complete and symmetrical. A precise and efficient method of lung segmentation is significant to the diagnosis of pectoral disease. Lung segmentation is a crucial first step for the consequential detection of many pectoral diseases, such as pulmonary nodules and diffuse pneumonia, and the method can play a role in this regard. All the parameters in the presented framework are adjusted on the liver dataset. We expect to fine-tune the framework and make it more fitting to the lung segmentation in the future. It could contribute to the higher accuracy on lung segmentation.

In addition, the structure of DL determines the running time reduction. The time consumed by the liver segmentation is 38 s/slice. For the left and right lungs segmentation, it takes 40 s/slice.

## Conclusions

This paper presents a CNN-based framework for multiple organs (liver and lung) segmentation from abdominal CT and HRCT scans. The CNN is improved by the super-pixel (SLIC) and SVM classifiers, which help reduce computational costs. The framework performs a desirable segmentation on the datasets that include livers and lungs. Overall, the processing time is cut, while precise segmentation results are obtained. In the future, we are committed to testing this framework on other kinds of organs. Improvement of accuracy and efficiency is also expected. We are looking forward to placing framework into clinical diagnosis that can benefit patients.

**Funding information** The research is supported by the China Science and Technology Program (2015DFA11180) and the Foundation of Jilin Development and Reform Commission (2015Y034-5).

## References

1. Moltz JH, Bornemann L, Dicken V: Segmentation of Liver Metastases in CT Scans by Adaptive Thresholding and Morphological Processing. *International Conference on Medical Image Computing and Computer-Assisted Intervention*. p. 195–222, 2008
2. Chang YL, Li X: Adaptive image region-growing. *IEEE Transactions on Image Processing* 3(6):868–872, 1994
3. Devi KG, Radhakrishnan R: Segmentation of multiple organ from abdominal CT images using 3D region growing and gradient vector flow. *International Journal of Applied Engineering Research* 9(24): 30023–30041, 2014
4. Toennies RPAKD: Segmentation of Medical Images Using Adaptive Region Growing. *Proceedings of SPIE Medical Imaging* 43(22):1337–1346, 2001
5. Oda M, Nakaoka T, Kitasaka T: Organ segmentation from 3d abdominal CT images based on atlas selection and graph cut. *International Conference on Abdominal Imaging. Computational and Clinical Applications*, p. 181–188, 2012

6. Luo S, Li X, Li J: Review on the Methods of Automatic Liver Segmentation from Abdominal Images. *Journal of Computer & Communications* 02(2):1–7, 2014
7. Jones JL, Xie X, Essa E: Combining region-based and imprecise boundary-based cues for interactive medical image segmentation. *International Journal for Numerical Methods in Biomedical Engineering* 30(12):1649–1666, 2014
8. Taha AA, Hanbury A: Metrics for evaluating 3D medical image segmentation: analysis, selection, and tool. *BMC Medical Imaging* 15(1):29, 2015
9. Zhou S, Wang J, Zhang S: Active contour model based on local and global intensity information for medical image segmentation. *Neurocomputing* 186(C):107–118, 2016
10. Zografos V, Valentinitich A, Rempfler M: Hierarchical multi-organ segmentation without registration in 3D abdominal CT images. *International Conference on Medical Image Computing and Computer-Assisted Intervention*, p. 37–46, 2016
11. Cuingnet R, Prevost R, Lesage D: Automatic detection and segmentation of kidneys in 3D CT images using random forests. *International Conference on Medical Image Computing and Computer-Assisted Intervention*, p. 66–74, 2012
12. Muhammad Moazam F, Remagnino P, Andreas H: An ensemble classification-based approach applied to retinal blood vessel segmentation. *IEEE transactions on bio-medical engineering* 59(9): 2538–2548, 2012
13. Lombaert H, Zikic D, Criminisi A: Laplacian Forests: semantic image segmentation by guided bagging. *International Conference on Medical Image Computing and Computer-Assisted Intervention*, p. 496–504, 2014
14. Shen D, Wu G, Suk HI: Deep Learning in Medical Image Analysis. *Annual Review of Biomedical Engineering*. 19:221, 2017
15. Shen W, Zhou M, Yang F: Multi-scale Convolutional Neural Networks for Lung Nodule Classification. *International Conference on Information Processing in Medical Imaging*, p. 588–99, 2015
16. Nie D, Zhang H, Adeli E: 3D Deep Learning for Multi-modal Imaging-Guided Survival Time Prediction of Brain Tumor Patients. *International Conference on Medical Image Computing and Computer-Assisted Intervention*, p. 212–220, 2016
17. Gerazov B, C.R.C., *Deep learning for tumour classification in homogeneous breast tissue in medical microwave imaging*. *IEEE Eurocon 2017 - International Conference on Smart Technologies*, 2017: p. 564–569
18. Shin HC, Orton MR, Collins DJ: Stacked autoencoders for unsupervised feature learning and multiple organ detection in a pilot study using 4D patient data. *IEEE Transactions on Pattern Analysis & Machine Intelligence* 35(8):1930–1943, 2013
19. Wang Z, Yang J: SU-F-J-04: Automated Detection of Diabetic Retinopathy Using Deep Convolutional Neural Networks. *Medical Physics* 43(6):3406–3406, 2016
20. Kooi T, Litgens G, Van Ginneken B: Large scale deep learning for computer aided detection of mammographic lesions. *Medical Image Analysis* 35:303–312, 2017
21. Sevastopolsky A: Optic disc and cup segmentation methods for glaucoma detection with modification of U-Net convolutional neural network. *Pattern Recognition and Image Analysis* 27:618–624, 2017
22. Mansoor A, Cerrolaza JJ, Perez G: Marginal Shape Deep Learning: Applications to Pediatric Lung Field Segmentation. *The International Society for Optical Engineering*, p. 10133, 2017
23. Sun C, Guo S, Zhang H: Automatic segmentation of liver tumors from multiphase contrast-enhanced CT images based on FCNs. *Artif Intell Med* 83:58–66, 2017
24. Lécun Y, Bottou L, Bengio Y: Gradient-based learning applied to document recognition. *Proceedings of the IEEE* 86(11):2278–2324, 1998
25. Kayalibay B, Jensen G, Smagt P V D: CNN-based Segmentation of Medical Imaging Data. *arXiv e-print (arXiv:1701.03056)*, 2017
26. Cha K, Hadjiiski L, Chan H P: Deep-Learning-based Bladder Segmentation in CT Urography. *Radiological Society of North America*, 2015
27. Zou Y, Li L, Wang Y: Classifying digestive organs in wireless capsule endoscopy images based on deep convolutional neural network. *IEEE International Conference on Digital Signal Processing*, p. 1274–1278, 2015
28. Jia Y, Shelhamer E, Donahue J: Caffe: Convolutional Architecture for Fast Feature Embedding. *ACM International Conference on Multimedia*, p. 675–678, 2014
29. Chang C C, Lin C J: LIBSVM: A library for support vector machines. *ACM Transactions on Intelligent Systems and Technology* 2(3):1–27, 2011
30. Heimann T, van Ginneken B, Styner MA: Comparison and Evaluation of Methods for Liver Segmentation From CT Datasets. *IEEE Transactions on Medical Imaging* 28(8):1251–1265, 2009
31. <https://tianchi.aliyun.com/competition/>. Accessed April 2017
32. Lim SJ, Jeong YY, Ho YS: Automatic liver segmentation for volume measurement in CT images. *Journal of Visual Communication & Image Representation* 17(4):860–875, 2006
33. Farag A, Lu L, Roth HR: A bottom-up approach for pancreas segmentation using cascaded superpixels and (deep) image patch labeling. *IEEE Transactions on Image Processing* 26(1):386–399, 2015
34. Achanta R, Shaji A, Smith K: SLIC Superpixels Compared to State-of-the-Art Superpixel Methods. *IEEE Transactions on Pattern Analysis & Machine Intelligence* 34(11):2274–2282, 2012
35. Vapnik VN: *Statistical Learning Theory*. Wiley, 1998
36. Krizhevsky A, Sutskever I, Hinton GE: ImageNet classification with deep convolutional neural networks. *International Conference on Neural Information Processing Systems*, p. 1097–1105, 2012
37. Dice LR: Measures of the amount of ecologic association between species. *Ecology* 26(3):297–302, 1945
38. Heimann T, van Ginneken B, Styner MA: Comparison and evaluation of methods for liver segmentation from CT datasets. *IEEE Transactions on Medical Imaging* 28(8):1251–1265, 2009
39. Ruskó L, Bekes G, Fidrich M: Automatic segmentation of the liver from multi- and single-phase contrast-enhanced CT images. *Medical Image Analysis* 13(6):871–882, 2009
40. Hu P, Wu F, Peng J: Automatic 3D liver segmentation based on deep learning and globally optimized surface evolution. *Physics in Medicine & Biology* 61(24):8676, 2016
41. Dou Q, Chen H, Jin Y: 3D deeply supervised network for automatic liver segmentation from CT volumes. *International Conference on Medical Image Computing and Computer-Assisted Intervention*, p. 149–157, 2016
42. Li G, Chen X, Shi F: Automatic liver segmentation based on shape constraints and deformable graph cut in CT images. *IEEE Transactions on Image Processing* 24(12):5315, 2015
43. Peng J, Hu P, Lu F: 3D liver segmentation using multiple region appearances and graph cuts. *Medical Physics* 42(12):6840–6852, 2015
44. Wu W, Zhou Z, Wu S: Automatic liver segmentation on volumetric CT images using supervoxel-based graph cuts. *Computational & Mathematical Methods in Medicine* 2016:9093721, 2016
45. Lu F, Wu F, Hu P: Automatic 3D liver location and segmentation via convolutional neural network and graph cut. *International Journal of Computer Assisted Radiology & Surgery* 12(2):171, 2017
46. Pulagam AR: K.G.B., Ede V K. *Automated lung segmentation from HRCT scans with diffuse parenchymal lung diseases*. *Journal of Digital Imaging* 29(4):507–519, 2016
47. Doganay E, Kart L, Özcelik HK: A robust lung segmentation algorithm using fuzzy C-means method from HRCT scans. *European Respiratory Journal* 48(suppl 60):PA750, 2016
48. Harrison A P, Xu Z., George K: Progressive and Multi-path Holistically Nested Neural Networks for Pathological Lung Segmentation from CT Images. *International Conference on Medical Image Computing and Computer-Assisted Intervention*, p. 621–629, 2017